A methodology for dynamic material characterizations via terahertz time-domain spectroscopy

Nikolai I. Lesack, Naomi V. Fredeen, *Student Member*, *IEEE*,
Andrew Jirasek, and Jonathan F. Holzman, *Member, IEEE*

***Abstract*—In this work, the challenges of terahertz (THz) time-domain spectroscopy on complex (multilayer) samples with time-varying (dynamic) characteristics are addressed. The challenges appear in characterizations of the refractive index and extinction coefficient, as etalon artefacts due to internal reflections, and are accentuated in multilayer structures having dynamic and low-loss materials, such as biomolecular materials. This is because nonidealities may form as airgaps at the interfaces and as inhomogeneity in the bulk. The proposed methodology addresses the challenges by introducing a generalized model that accommodates dynamic formation of airgaps and inhomogeneity. It is shown that the generality of the model allows it to mitigate etalon artefacts and yield a highly accurate representation of the material characteristics, with low systematic error, even for low-loss materials. The methodology is applied to characterizations of quartz and glucose in the THz spectrum to see fine detail in the characteristics of quartz and the crystallization of glucose.**

***Index Terms*—Absorption, electromagnetic wave propagation, refraction, signal processing, spectroscopy, terahertz time-domain spectroscopy, dynamic material characterization.**

I. Introduction

THE terahertz (THz) spectrum is a rich resource for spectroscopic analyses. Terahertz spectroscopy utilizes low frequencies (from 0.3 to 3.0 THz), with low photon energies (from 1.2 to 12 meV), to glean details on both the fine signatures of intramolecular absorption [1]–[3] and the broadband expression of intermolecular interactions [2]–[4]. Such capabilities have supported its use in THz time-domain spectroscopy (THz-TDS) of many biomolecular compounds, including saccharides [3]–[7] proteins [8], [9], and lipids [10], [11], as well as various inorganic compounds in vapour [12], [13], liquid [14], [15], or solid [14], [16] forms.

While THz-TDS analyses have generated a deeper understanding for many materials, by revealing their refractive indices and extinction coefficients, such analyses must consider the manifestation of random and systematic error. Random error is a metric of precision and is defined by deviations between measured values. To reduce random error, prior THz-TDS analyses have employed techniques such as the Moving Mean Filter [16] and Spatial Variant Moving Average Filter [15], [17]. Nonetheless, such filtering serves to minimize nondeterministic fluctuations, and so it can be reduced to a suitable level by simply averaging a sufficient number of measurements. However, this is not the case for systematic error. Systematic error is a metric of accuracy and is defined by deviations between measured values and the true value. The main source of systematic error in THz-TDS analyses is the etalon artefacts that result from reflections within the sample's layers[1]. These etalons must be accurately defined in the model to have their artefacts not appear in the extracted refractive index and extinction coefficient.

There are two general methods to remove etalon artefacts. The first, Time-Domain Peak Subtraction Method [19], uses a time-domain model and measured layer thicknesses to extract the material characteristics. It yields reasonable accuracy, as quantified in Table I. The second, Inversion Method [15]–[17], [20]–[24], uses a frequency-domain model and measured

Manuscript received August ??, 2019; revised September ??, 2019; accepted October ??, 2019. Date of publication November ??, 2019; date of current version August ??, 2019. This work was supported in part by the Natural Sciences and Engineering Research Council of Canada (NSERC) grant numbers RGPIN-2017-04073 and RGPIN-2015-04744, the Canadian Foundation for Innovation (CFI) grant number LOF 16659, the Canadian Institute of Health Research (CIHR) grant number 258926, and Western Economic Diversification Canada (WD).

N. V. Fredeen and J. F. Holzman are with the School of Engineering, University of British Columbia, Kelowna, BC, V1V 1V7, Canada (e-mail: nvfredeen@gmail.com; jonathan.holzman@ubc.ca).

N. I. Lesack and A. Jirasek are with the Irving K. Barber School of Arts and Sciences, University of British Columbia, Kelowna, BC, V1V 1V7, Canada (e-mail: nikolai.lesack@alumni.ubc.ca; andrew.jirasek@ubc.ca).

Color versions of one or more of the figures in this paper are available online at http://ieeexplore.ieee.org.

Digital Object Identifier 10.1109/TTHZ.2020.2972945

[1] In general, according to [18], systematic errors can be categorized as errors in the measured sample thickness, errors from approximations of the theoretical transfer function, errors from registration noise and mechanical drift, errors in sample alignment, and errors from environmental parameters. The first two errors manifest as etalon artefacts. They can be reduced by using a sufficiently general theoretical model of the sample, which characterizes reflections from all of the interfaces and treats the refractive indices, extinction coefficients, and thicknesses of all the layers as fitting parameters. Such an approach is used in this work by way of its generalized model. The remaining three errors can be reduced by careful experimental procedures. Errors from registration noise and mechanical drift can be reduced by having sufficient (submicron) accuracy for the THz system's translation stage. Errors in sample alignment can be diminished by having sufficient precision (within 2° [18]) for mounts. Errors from environmental parameters can be mitigated by having a sufficiently short (below 30 cm) propagation length for the THz beam. These experimental procedures are applied in this work.

TABLE I
SYSTEMATIC ERRORS FOR METHODS AND/OR ALGORITHMS IN THE LITERATURE

Method and/or Algorithm	Systematic errors in the refractive index	Reference
Time-Domain Peak Subtraction Method	0.06–0.1 (estimated)	[19]
Inversion Method	0.02–0.1 (estimated)	[16]
Inversion Method	0.002–0.005	[20]
Total Variation Algorithm	0.01	[21]
Total Variation Algorithm	0.01–0.03 (estimated)	[22]
Total Variation Algorithm	0.006–0.02 (estimated)	[17]
Total Variation Algorithm	0.004	[15]
Quasi Space Algorithm	0.002-0.01	[25]

layer thicknesses to extract the same characteristics. It yields reasonable to excellent accuracy, as quantified in Table I. Nevertheless, these general methods have strong sensitivity to the measured layers' thicknesses, in that small errors can yield large systematic error and prominent etalon artefacts. For this reason, the methods have been augmented by the Total Variation Algorithm [15], [17], [21], [22] and Quasi Space Algorithm [25], [26], [27]. The former algorithm treats the layers' thicknesses as fitting parameters whose values are tuned to minimize etalon artefacts within the extracted material characteristics. This yields reasonable to excellent accuracy, as quantified in Table I. The latter algorithm also varies the layers' thicknesses, as fitting parameters, although it does so by identifying and minimizing the etalon artefacts that form as discrete peaks in a transformed (quasi) space. It yields excellent accuracy, as quantified in Table I.

Ultimately, all the above methods and algorithms are related by their reliance upon idealizations for the layers' interfaces and homogeneity. While such idealizations may be true for static material characterizations, they may not be true for dynamic material characterizations [19], [28]. As stated by van Mechelen *et al*., amongst others, THz-TDS analyses of complex structures (i.e., multilayer samples) with time-varying properties (i.e., dynamic characteristics) often break down or lack accuracy [29]. The proposed work targets this challenge for dynamic material characterizations.

In this work, a rigorous THz-TDS methodology is presented for dynamic material characterizations. The methodology contrasts theoretical characteristics, from a generalized model of a multilayer sample, to experimental characteristics, having been measured in a sequence that isolates and characterizes the sample's individual layers. The model encompasses all of the layers' internal reflections as well as time-varying nonidealities for the layers' interfaces and bulk, which manifest as airgaps and inhomogeneity, respectively. It is shown that the generalized model and experimental process together diminish the etalon artefacts – even for samples with low-loss materials. This reduces the systematic errors below those of an idealized model, which considers internal reflections but does not consider the aforementioned time-varying nonidealities. The THz-TDS methodology is demonstrated by way of dynamic material characterizations of crystallization in glucose.

II. Terahertz Time-Domain Spectroscopy

The proposed THz-TDS methodology is defined in this section for a generalized model of a multilayer sample. The multilayer sample has a target layer, for which the material characteristics are sought, between two support layers. It is assumed that the characteristics of the support layers are static, but the characteristics of the target layer may be dynamic. This can lead to two nonidealities for the target layer. The first nonideality relates to airgaps at the interfaces. These airgaps are encompassed in the generalized model by treating their thicknesses as fitting parameters, with a thickness of zero resulting if an airgap is absent. The second nonideality relates to inhomogeneity across the target layer. It is encompassed in the generalized model by a variational parameter, δ, which acts as an empirical perturbation factor to the idealized model. The physicality of this parameter will be discussed later. The complete multilayer sample has five indexed layers, with indices i = 1 and 5 denoting the (static and homogenous) support layers, index i = 3 denoting the (dynamic and inhomogeneous) target layer, and indices i = 2 and 4 denoting (potential) airgaps. Ultimately, the theoretical characteristics arising from the generalized model of this multilayer sample are contrasted to experimental characteristics.

Two types of experimental characteristics are acquired in the THz-TDS methodology. There are characteristics of the support layers, in isolation, and characteristics of the fully-assembled multilayer sample. The characteristics are acquired by measuring the THz sample waveform, $E_s(t)$, that emerges through the layer(s) and computing its THz sample spectrum, $\tilde{E}_s(f)$, via Fourier transform. The THz reference waveform, $E_r(t)$, and its spectrum, $\tilde{E}_r(f)$, are acquired after propagating through free-space over the net thickness of the layer(s). We assume here that the THz waveforms are all polarized in the same direction, so vector notation is not needed nor used to denote field quantities in this work. The overhead tildes simply denote complex-valued phasors.

The spectra have harmonic dependence on time, t, and frequency, f, in the form of $e^{j2\pi ft} = e^{jk_0 ct}$, where $k_0 = 2\pi f/c$ is the magnitude of the free-space wavevector and c is the free-space speed of light. For each support layer, indexed by i = 1 and 5, the experimental characteristics are defined by a *transmission ratio* of $[\tilde{E}_s(f)/\tilde{E}_r(f)]_i$ and the theoretical characteristics are defined by a *transmission function* of $\tilde{H}_i(f)e^{jk_0 d_i}$, where $\tilde{H}_i(f)$ is the transfer function across the layer and $e^{jk_0 d_i}$ is a complex exponential quantifying the free-space phase shift across the layer's thickness, d_i. For the fully-assembled multilayer sample, indexed by i = 1–5, the experimental characteristics are defined by a *transmission ratio* of $[\tilde{E}_s(f)/\tilde{E}_r(f)]_{1-5}$ and the theoretical characteristics are defined by a *transmission function* of $\tilde{H}_{1-5}(f)e^{jk_0 d_{1-5}}$, where $\tilde{H}_{1-5}(f)$ is the transfer function across the layers and $e^{jk_0 d_{1-5}}$ is a complex exponential quantifying the free-space phase shift across the layers' net thickness of $d_{1\text{-}5} = d_1 + \ldots + d_5$.

The above theoretical and experimental characteristics are contrasted in characteristic equations to extract the desired optical and structural parameters. The characteristic equations for the support layers,

$$\tilde{H}_i(f)e^{\mathrm{j}k_0 d_i} - \left[\frac{\tilde{E}_\mathrm{s}(f)}{\tilde{E}_\mathrm{r}(f)}\right]_i = 0, \quad (1)$$

are defined by i = 1 and 5. The equations are solved by inserting into the first term the theoretical transmission function for both layers, as derived in subsection II.A, and inserting into the second term the experimental transmission ratio measured for both layers, using the setup introduced in subsection II.B. For a given layer i, the difference between the terms is set to zero, yielding distinct equations for the real and imaginary components at each frequency. The two equations, corresponding to the real and imaginary equations, are solved simultaneously for the two unknowns, being the refractive index and extinction coefficient, while stepping through the frequency. Etalon artefacts are identified in the spectra for the refractive index and extinction coefficient and then minimized by varying the layer's thickness, as described in subsection II.C. The characteristic equation of the multilayer sample,

$$\tilde{H}_{1\text{–}5}(f)e^{\mathrm{j}k_0 d_{1\text{–}5}} - \left[\frac{\tilde{E}_\mathrm{s}(f)}{\tilde{E}_\mathrm{r}(f)}\right]_{1\text{–}5} = 0\,. \quad (2)$$

is defined by i = 1–5. The equation is solved with attention to its known and unknown parameters. Its known parameters are the refractive indices, extinction coefficients, and thicknesses defined earlier for the support layers, as well as the refractive index and extinction coefficient of the airgaps, whose values are assumed to be unity and zero, respectively. Its unknown parameters are the sought refractive index, extinction coefficient, and thickness of the target layer, the thicknesses of the airgaps, and the variational parameter, δ. As such, (2) is solved by inserting into the first term the expression for the theoretical transmission function of the multilayer sample, as derived in subsection II.A, and by inserting into the second term the experimental transmission ratio measured for the multilayer sample, using the setup introduced in subsection II.B. As described above, the difference of the terms is set to zero, for both the real and imaginary components, and the values for the three unknown parameters of the target layer, thicknesses of the airgaps, and variational parameter, δ, are extracted using the methodology presented in subsection II.C.

A. Theoretical Characteristics: The Transmission Function

In this subsection, we consider the theoretical characteristics for THz wave propagation through a sample. We use an adapted form of the Inversion Method to define transmission functions for the support layers and multilayer sample, as seen in the characteristic equations (1) and (2). The Inversion Method is chosen over the Time-Domain Peak Subtraction Method because our experience shows that it better resolves the sharp spectral features arising from low-loss materials, being the focus of this work.

We consider the THz wave propagation through a general layer i. The layer has a thickness of d_i and a complex refractive index of $\tilde{n}_i(f) = n_i(f) - \mathrm{j}\kappa_i(f)$, where $n_i(f)$ is the refractive index and $\kappa_i(f)$ is the extinction coefficient. (The extinction coefficient can be transformed, as necessary, to a corresponding (power) absorption coefficient as $\alpha_i(f) = 2k_0\kappa_i(f)$.) Propagation through the layers is modelled in accordance with standardized theory for electromagnetic wave propagation through multilayer structures [30], given reflection and transmission at the interfaces as well as phase delay and absorptive loss across the layers. For propagation across the interface from layer i into layer $i + 1$, the ratio of transmitted to incident electric field phasors is defined by the transmission coefficient $\tilde{t}_{i,i+1}(f) = 2\,\tilde{n}_i(f)/(\tilde{n}_i(f)+\tilde{n}_{i+1}(f))$ and the ratio of reflected to incident electric field phasors is defined by the reflection coefficient $\tilde{r}_{i,i+1}(f) = (\tilde{n}_i(f)-\tilde{n}_{i+1}(f))/(\tilde{n}_i(f)+\tilde{n}_{i+1}(f))$. Note that the subscripts i and $i + 1$ here can be set to 0 to have them apply to free space beyond the entrance and exit interfaces.

Reflection, transmission, phase delay, and absorptive loss for the support layers, indexed by i = 1 and 5, are quantified by the reflection coefficient $\tilde{\Gamma}_i(f)$ and transfer function $\tilde{H}_i(f)$ via

$$\begin{aligned}\begin{bmatrix}1\\ \tilde{\Gamma}_i(f)\end{bmatrix} &= \mathbf{B}_{0,i}\,\mathbf{P}_i\,\mathbf{B}_{i,0}\begin{bmatrix}\tilde{H}_i(f)\\ 0\end{bmatrix}\\ &= \frac{1}{\tilde{t}_{0,i}(f)\tilde{t}_{i,0}(f)}\begin{bmatrix}1 & \tilde{r}_{0,i}(f)\\ \tilde{r}_{0,i}(f) & 1\end{bmatrix}\begin{bmatrix}e^{\mathrm{j}k_0\tilde{n}_i(f)d_i} & 0\\ 0 & e^{-\mathrm{j}k_0\tilde{n}_i(f)d_i}\end{bmatrix}\\ &\quad \begin{bmatrix}1 & \tilde{r}_{i,0}(f)\\ \tilde{r}_{i,0}(f) & 1\end{bmatrix}\begin{bmatrix}\tilde{H}_i(f)\\ 0\end{bmatrix}.\end{aligned} \quad (3)$$

Following the well-established matrix-based method, seen in [30], $\mathbf{B}_{i,i+1}$ and $\mathbf{P}_i$ are the reflection and propagation matrices for propagation across the interface from layer i to $i+1$ and propagation across layer i, respectively. Ultimately, the transfer function $\tilde{H}_i(f)$ in (3) is solved for and multiplied by $e^{\mathrm{j}k_0 d_i}$ to define the transmission function of layer i for use in (1). It takes on the well-known form of $\tilde{H}_1(f)e^{\mathrm{j}k_0 d_1} = \tilde{t}_{0,1}(f)\;\tilde{t}_{1,0}(f)\;e^{-\mathrm{j}k_0(\tilde{n}_1(f)-1)d_1}\,/\,(1+\tilde{r}_{0,1}(f)\tilde{r}_{1,0}(f)e^{-\mathrm{j}k_0\tilde{n}_1(f)2d_1})$ [20], [31].

Reflection, transmission, phase delay, and absorptive loss in the multilayer sample, i = 1–5, are quantified by the reflection coefficient $\tilde{\Gamma}_{1\text{–}5}(f)$ and transfer function $\tilde{H}_{1\text{–}5}(f)$ via

$$\begin{bmatrix} 1 \\ \tilde{\Gamma}_{1-5}(f) \end{bmatrix} = \mathbf{B}_{0,1}\,\mathbf{P}_1\,\mathbf{B}_{1,2}\cdots\mathbf{B}_{4,5}\,\mathbf{P}_5\,\mathbf{B}_{5,0}\begin{bmatrix} \tilde{H}_{1-5}(f) \\ 0 \end{bmatrix}$$
$$= \frac{(\delta+1)^{-2}}{\prod_{i=1}^{5}\tilde{t}_{i-1,i}\;\tilde{t}_{5,0}}\begin{bmatrix} 1 & \tilde{r}_{0,1}(f)(\delta-1) \\ \tilde{r}_{0,1}(f)(\delta-1) & 1 \end{bmatrix}$$
$$\begin{bmatrix} e^{jk_0\tilde{n}_1(f)d_1} & 0 \\ 0 & e^{-jk_0\tilde{n}_1(f)d_1} \end{bmatrix}\begin{bmatrix} 1 & \tilde{r}_{1,2}(f) \\ \tilde{r}_{1,2}(f) & 1 \end{bmatrix}\cdots \quad (4)$$
$$\begin{bmatrix} 1 & \tilde{r}_{4,5}(f) \\ \tilde{r}_{4,5}(f) & 1 \end{bmatrix}\begin{bmatrix} e^{jk_0\tilde{n}_5(f)d_5} & 0 \\ 0 & e^{-jk_0\tilde{n}_5(f)d_5} \end{bmatrix}$$
$$\begin{bmatrix} 1 & \tilde{r}_{5,0}(f)(\delta-1) \\ \tilde{r}_{5,0}(f)(\delta-1) & 1 \end{bmatrix}\begin{bmatrix} \tilde{H}_{1-5}(f) \\ 0 \end{bmatrix}.$$

Here, the transfer function $\tilde{H}_{1-5}(f)$ in (4) is solved for and multiplied by $e^{jk_0d_{1-5}}$ to define the transmission function of the multilayer sample for use within (2). Note that the entrance and exit interfaces have multiplicative factors of $(\delta+1)$ and $(\delta-1)$ out front of their transmission and reflection coefficients, respectively. These factors apply the variational parameter, δ, to quantify the level of inhomogeneity across the target layer. Our prior studies have shown that such inhomogeneity can cause variances between the theoretical and experimental characteristics, which yield an etalon artefact in the extracted refractive indices and extinction coefficients at the free spectral range of the outermost cavity. This etalon artefact, albeit small, cannot be removed by any combination of values for the optical and structural fitting parameters in the model. It is shown later that the inclusion and fitting of this variational parameter, δ, can remove this unyielding etalon artefact.

B. Experimental Characteristics: The Transmission Ratio

The THz-TDS system that measures the needed THz sample spectra and THz reference spectra, and thus defines the transmission ratios, is shown in Fig. 1. It makes use of an ultrafast pulsed laser (Toptica Photonics Inc., FFS-SYS-2B) with a wavelength of 775 nm, repetition rate of 90 MHz, and pulse duration of 100 fs. The pulsed output from the laser is divided by a beamsplitter into pump and probe beams. The pump beam is directed onto a translation stage to impart a time delay onto its pulses and then directed onto a THz emitter (Ekspla Inc., EMT-08) in the form of a biased stripline antenna. The probe beam is directed onto a THz detector (Ekspla Inc., DET-08) in the form of a biased dipole antenna. The THz electric field that is detected is recorded as a function of the relative time delay between the pump and probe pulses. This is done with the sample in the path of the THz beam, yielding the THz sample waveform, $E_s(t)$, and without the sample in the path of the THz beam, yielding the THz reference waveform, $E_r(t)$. The waveforms are then Fourier transformed to define the THz sample spectrum, $\tilde{E}_s(f)$, and THz reference waveform, $\tilde{E}_r(f)$, respectively.

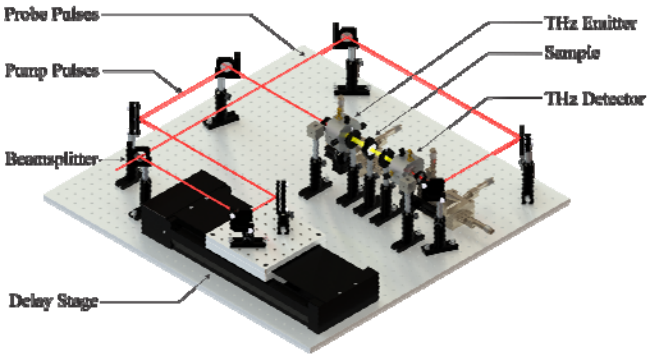

Fig. 1. Schematic of the experimental THz-TDS system. Laser pulses from the ultrafast pulsed laser are split by the displayed beamsplitter into trains of pump pulses and probe pulses. The pump pulses are delayed by the delay stage and then directed onto the THz emitter. The probe pulses are directed onto the THz detector. Radiation from the THz emitter propagates through the sample of interest and onto the THz detector.

C. Contrasting the Theoretical and Experimental Characteristics: The Methodology

The THz-TDS methodology contrasts the aforementioned theoretical and experimental characteristics for the support layers and fully-assembled multilayer sample.

The methodology used to solve the characteristic equation (1) for support layer i = 1 and 5 is depicted in the flowchart of Fig. 2(a). The experimental transmission ratio $[\tilde{E}_s(f)/\tilde{E}_r(f)]_i$ is taken as the input, and a numerical (MATLAB-based) root-solver is used to output the complex refractive index, $\tilde{n}_i(f) = n_i(f) - j\kappa_i(f)$. The root-solver yields values of the unknown parameters, being the refractive index, $n_i(f)$, extinction coefficient, $\kappa_i(f)$, and thickness, d_i, that have the real and imaginary components of the characteristic equation go to zero concurrently, at a tolerance of 10^{-12}. It uses literature values for its initial estimates of the refractive index and extinction coefficient and a measured value for its initial thickness, at a tolerance of 20 µm. The root-solver quantifies etalon artefacts throughout this process by using an adapted form of the Quasi Space Algorithm. This algorithm is chosen over the Total Variation Algorithm because it is better able to extract the thickness of a target layer with high accuracy – due to its ability to identify and minimize spectral features arising from internal reflections [27]. It does so by noting that an etalon artefact appears as sinusoidal ringing in the spectrum of the refractive index, $n_i(f)$, and extinction coefficient, $\kappa_i(f)$, with a period defined by the layer's free spectral range, $c/(2n_i(f)d_i)$. The severity of the artefact is quantified by taking the inverse Fourier transform of the optical parameters, which has each sinusoid map to a discrete etalon peak in the (quasi space) time-domain. The root-solver records the amplitudes of the etalon peaks for each set of parameter values that solve the characteristic equation and extracts the parameter values that yield the minimal amplitude. These extracted values for the layer's refractive index, $n_i(f)$, and extinction coefficient, $\kappa_i(f)$, exhibit the smallest etalon artefacts and thus the truest representation of the material characteristics. The extracted value of the thickness, d_i, is typically close to its initial estimate, although its role as an unknown parameter is important. Slight variations can yield prominent etalon

[20] L. Duvillaret, F. Garet, and J.-L. Coutaz, "A reliable method for extraction of material parameters in terahertz time-domain spectroscopy," *IEEE J. Sel. Top. Quantum Electron.*, vol. 2, no. 3, pp. 739–746, Sep. 1996, DOI: 10.1109/2944.571775.
[21] L. Duvillaret, F. Garet, and J. Coutaz, "Highly precise determination of optical constants and sample thickness in terahertz time-domain spectroscopy," *Appl. Opt.*, vol. 38, no. 2, pp. 409–415, Jan. 1999, DOI: 10.1364/AO.38.000409.
[22] T. D. Dorney, R. G. Baraniuk, and D. M. Mittleman, "Material parameter estimation with terahertz time-domain spectroscopy," *J. Opt. Soc. Am. A.*, vol. 18, no. 7, pp. 1562–1571, Jul. 2001, DOI: 10.1364/JOSAA.18.001562.
[23] K. Krewer, Z. Mics, J. Arabski, G. Schmerber, E. Beaurepaire, M. Bonn, and D. Turchinovich, "Accurate terahertz spectroscopy of supported thin films by precise substrate thickness correction," *Opt. Lett.*, vol. 43, no. 3, pp. 447–450, Feb. 2018, DOI: 10.1364/OL.43.000447.
[24] K. Su, Y. Shen, and J. A. Zeitler, "Terahertz sensor for non-contact thickness and quality measurement of automobile paints of varying complexity," *IEEE Trans. Terahertz Sci. Technol.*, vol. 4, no. 4, pp. 432–439, Jul. 2014, DOI: 10.1109/TTHZ.2014.2325393.
[25] M. A. Scheller, C. Jansen, and M. Koch, "Analysing sub-100-µm samples with transmission terahertz time domain spectroscopy," *Opt. Commun*, vol. 282, no. 7, pp. 1304–1306, Apr. 2009, DOI: 10.1016/j.optcom.2008.12.061.
[26] P. M. Glancy, "Terahertz time domain spectroscopy (THz-TDS) of hydrated biomolecular polymers and monomers," Ph.D. dissertation, Dept. Phys., U.C. Riverside., Riverside, CA, USA, 2009.
[27] X. Chen and E. Pickwell-MacPherson, "A sensitive and versatile thickness determination method based on non-inflection terahertz property fitting," *Sensors*, vol. 19, no. 19, pp. 4118, Oct. 2019, DOI: 10.3390/s19194118.
[28] A. I. McIntosh, B. Yang, S. M. Goldup, M. Watkinson, and R. S. Donnan, "Crystallization of amorphous lactose at high humidity studied by terahertz time domain spectroscopy," *Chem. Phys. Lett.*, vol. 558, pp. 104–108, Feb. 2013, DOI: 10.1016/j.cplett.2012.12.044.
[29] J. L. M. van Mechelen, A. B. Kuzmenko, and H. Merbold, "Stratified dispersive model for material characterization using terahertz time-domain spectroscopy," *Opt. Lett.*, vol. 39, no. 13, pp. 3853–3856, Jul. 2014, DOI: 10.1364/OL.39.003853.
[30] P. Yeh, "Optical Waves in Layered Media," New York, NY, USA: Wiley, 1988, pp. 102–114.
[31] R. Fastampa, L. Pilozzi, and M. Missori, "Cancellation of fabry-perot interference effects in terahertz time-domain spectroscopy of optically thin samples," *Phys. Rev. A: At. Mol. Opt. Phys*., vol. 95, no. 6, Jun. 2017, Art. no. 063831, DOI: 10.1103/PhysRevA.95.063831.
[32] S. Krimi, J. Klier, J. Jonuscheit, G. von Freymann, R. Urbansky, and R. Beigang, "Highly accurate thickness measurement of multi-layered automotive paints using terahertz technology," *Appl. Phys. Lett.*, vol. 109, no. 2, pp. 21105, Jul. 2016, DOI: 10.1063/1.4955407.
[33] M. Naftaly and R. E. Miles, "Terahertz time-domain spectroscopy: A new tool for the study of glasses in the far infrared." *J. Non-Cryst. Solids*, vol. 351, no. 40, pp. 3341-3346, Oct. 2005, DOI: 10.1016/j.jnoncrysol.2005.08.003.
[34] B. Makower and W. B. Dye, "Sugar crystallization, equilibrium moisture content and crystallization of amorphous sucrose and glucose," *J. Agric. Food. Chem.*, vol. 4, no. 1, pp. 72–77, Jan. 1956, DOI: 10.1021/jf60059a010.
[35] S. Söderholm, Y. H. Roos, N. Meinander, and M. Hotokka, "Raman spectra of fructose and glucose in the amorphous and crystalline states," *J. Raman Spectrosc*., vol. 30, no. 11, pp. 1009–1018, Nov. 1999. DOI: 10.1002/(SICI)1097-4555(199911)30:11<1009::AID-JRS436>3.0.CO;2-#

TABLE I

SYSTEMATIC ERRORS FOR METHODS AND/OR ALGORITHMS IN THE LITERATURE

Method and/or Algorithm	Systematic errors in the refractive index	Reference
Time-Domain Peak Subtraction Method	0.06–0.1 (estimated)	[19]
Inversion Method	0.02–0.1 (estimated)	[16]
Inversion Method	0.002–0.005	[20]
Total Variation Algorithm	0.01	[21]
Total Variation Algorithm	0.01–0.03 (estimated)	[22]
Total Variation Algorithm	0.006–0.02 (estimated)	[17]
Total Variation Algorithm	0.004	[15]
Quasi Space Algorithm	0.002-0.01	[25]

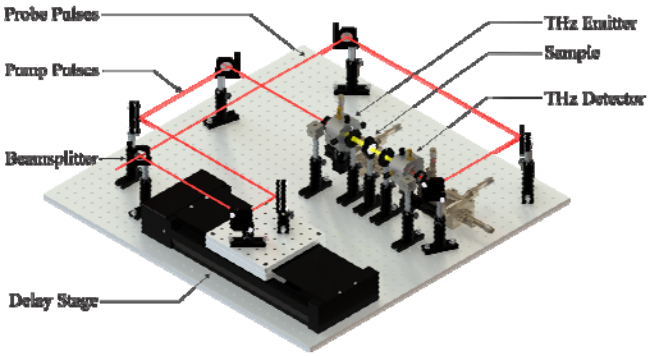

Fig. 1. Schematic of the experimental THz-TDS system. Laser pulses from the ultrafast pulsed laser are split by the displayed beamsplitter into trains of pump pulses and probe pulses. The pump pulses are delayed by the delay stage and then directed onto the THz emitter. The probe pulses are directed onto the THz detector. Radiation from the THz emitter propagates through the sample of interest and onto the THz detector.

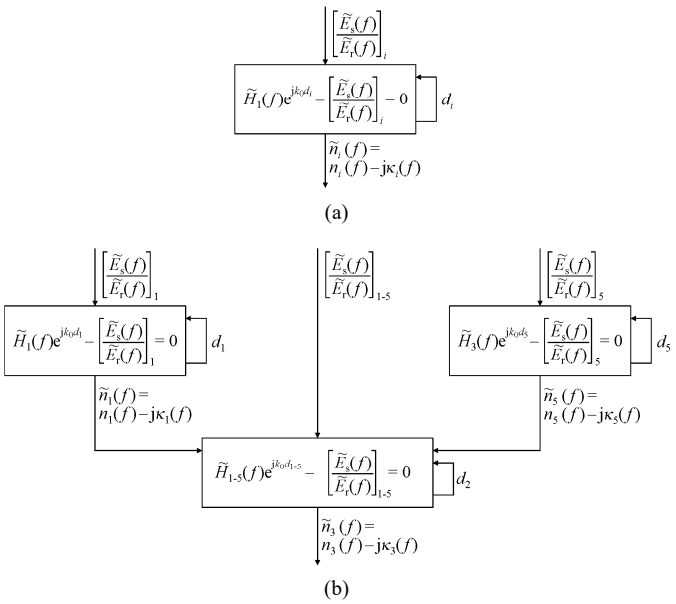

Fig. 2. The THz-TDS methodology is illustrated as flowcharts for the (a) support layer and (b) multilayer sample. In (a), the input is the transmission ratio of the support layer, and the output is its complex refractive index. In (b), the inputs are the transmission ratios of the two support layers and the multilayer sample, and the output is the complex refractive index of the target layer.

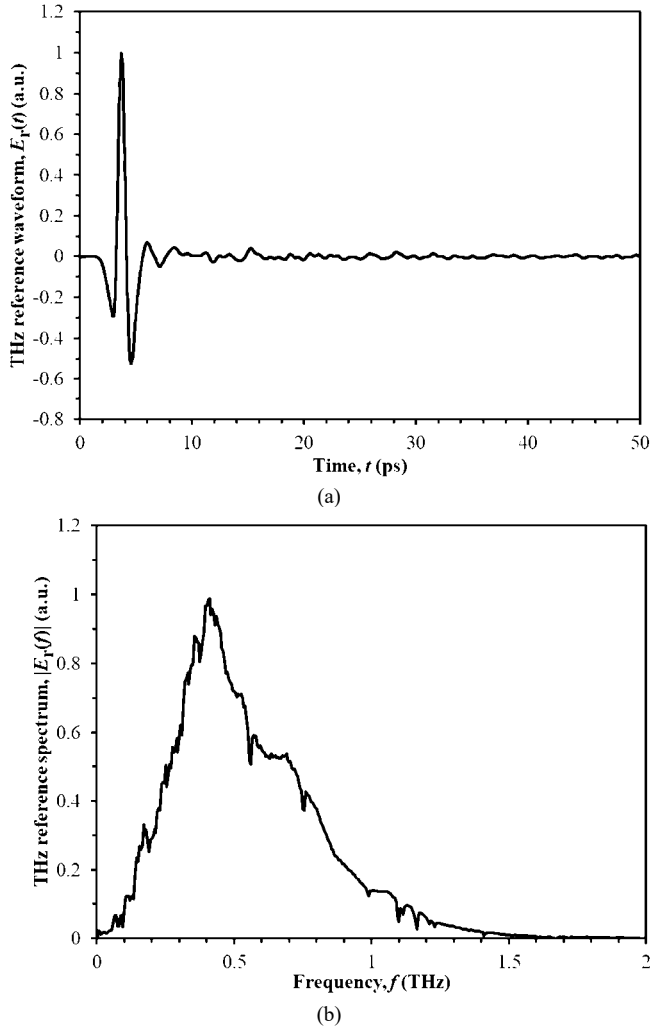

Fig. 3. Representative experimental results for (a) the THz reference waveform in the time-domain and (b) the corresponding THz reference spectrum (amplitude) in the frequency-domain.

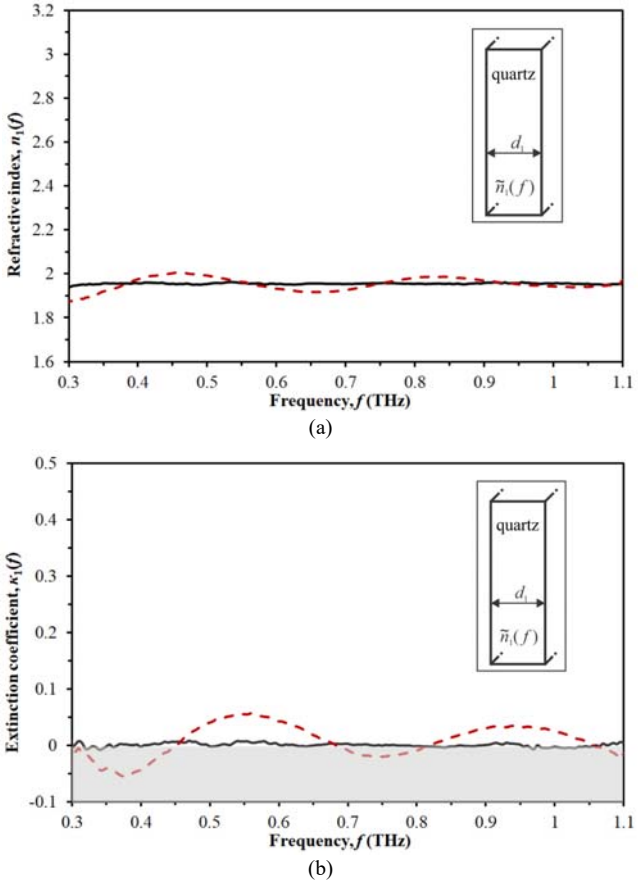

Fig. 4. Experimental results from THz-TDS analyses of a static support layer (quartz), as illustrated in the inset. The results show the (a) refractive index, $n_1(f)$, and (b) extinction coefficient, $\kappa_1(f)$. Solid black curves correspond to the generalized model of the theoretical transmission function, which characterizes all internal reflections; dashed red curves correspond to a naïve model of the theoretical transmission function, which does not characterize internal reflections. The negative range in (b) is shown in grey because it is unphysical.

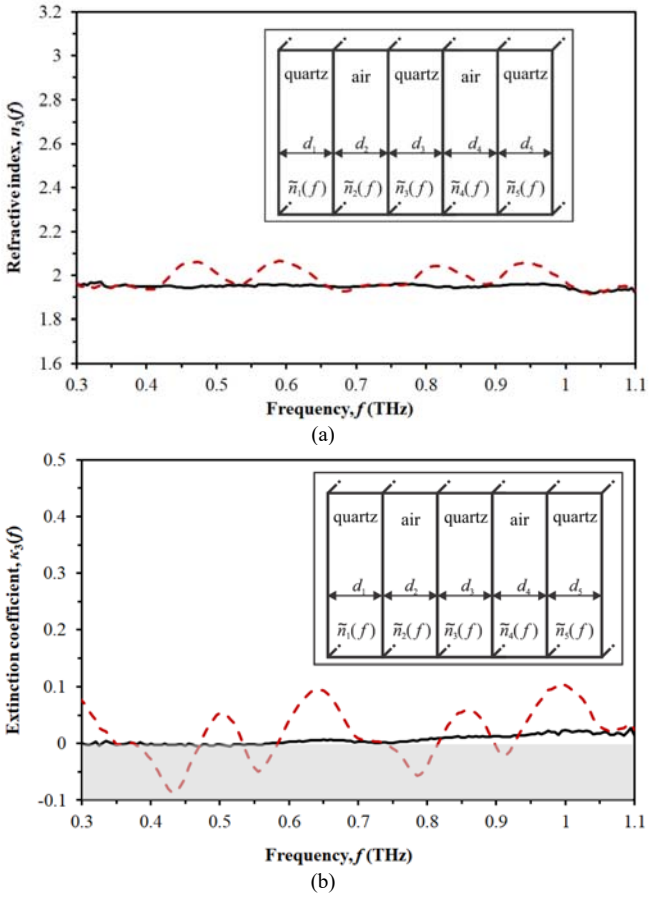

Fig. 5. Experimental results from THz-TDS analyses of a static multilayer sample (quartz-air-quartz-air-quartz), as illustrated in the inset. The results show the (a) refractive index, $n_3(f)$, and (b) extinction coefficient, $\kappa_3(f)$. Solid black curves show results from the generalized model of the theoretical transmission function, which characterizes all internal reflections as well as nonidealities in the form of airgaps at the interfaces and inhomogeneity in the bulk; dashed red curves show results from an idealized model, which characterizes all internal reflections but does not consider these nonidealities. The negative range in (b) is shown in grey because it is unphysical.

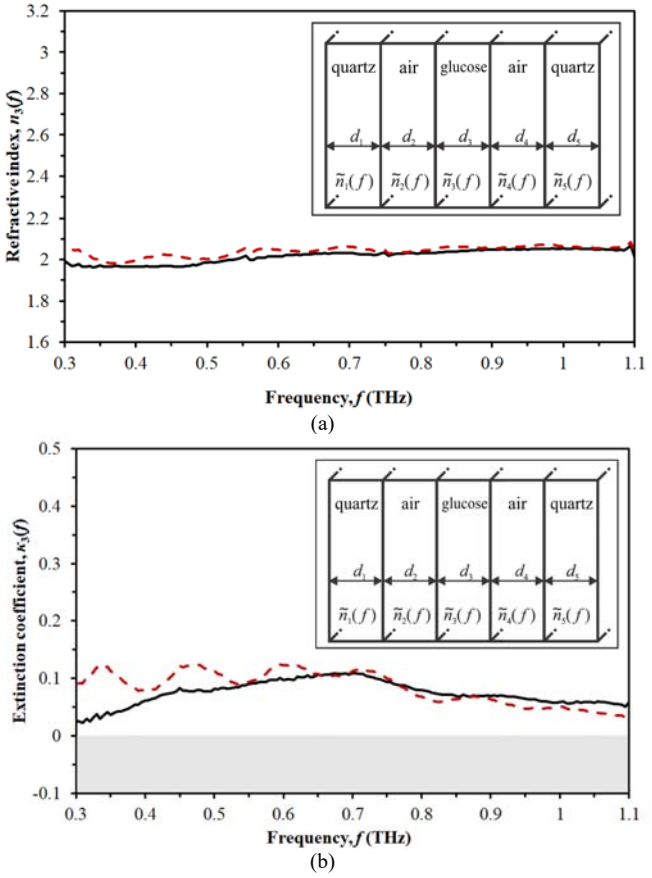

Fig. 6. Experimental results from THz-TDS analyses of a dynamic multilayer sample (quartz-air-glucose-air-quartz), as illustrated in the inset, at 90 hours. The results show the (a) refractive index, $n_3(f)$, and (b) extinction coefficient, $\kappa_3(f)$. Solid black curves show results from the generalized model of the theoretical transmission function, which characterizes all internal reflections as well as nonidealities in the form of airgaps at the interfaces and inhomogeneity in the bulk; dashed red curves show results from an idealized model, which characterizes all internal reflections but does not consider these nonidealities. The negative range in (b) is shown in grey because it is unphysical. Peaks appearing at 0.56, 0.75, 0.98, and 1.09 THz are due to water vapour absorption.

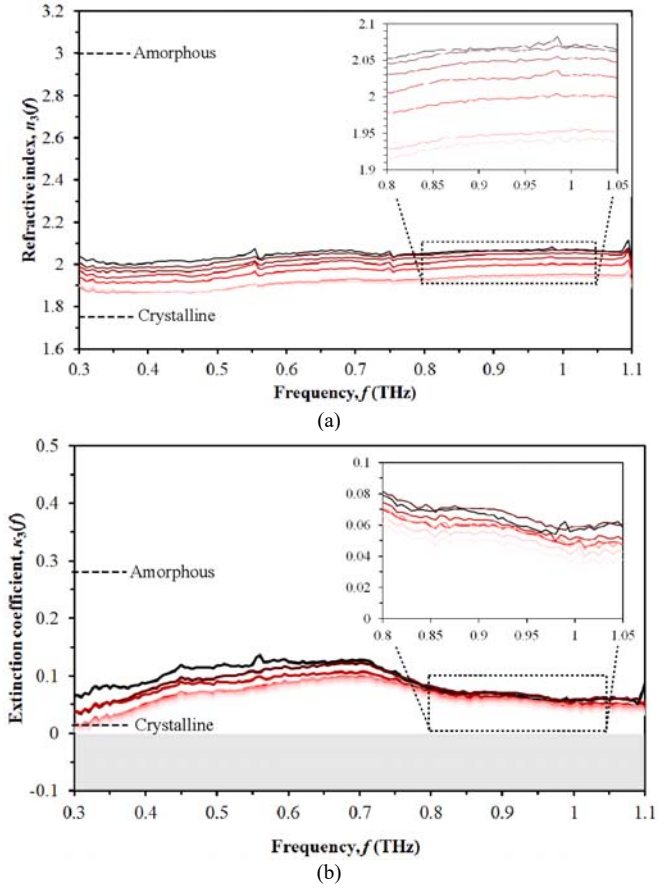

Fig. 7. Experimental results from THz-TDS analyses of a dynamic multilayer sample (quartz-air-glucose-air-quartz) at times of 60, 70, 80, 90, 100, 110, and 120 hours, as displayed from top to bottom. The results show the (a) refractive index, $n_3(f)$, and (b) extinction coefficient, $\kappa_3(f)$. An expanded view of the spectra from 0.8 to 1.05 THz is shown in the inset. The negative range in (b) is shown in grey because it is unphysical. Peaks appearing at 0.56, 0.75, 0.98, and 1.09 THz are due to water vapour absorption. The values of the refractive index and extinction coefficient for amorphous and polycrystalline glucose at 0.7 THz from [5] are indicated on the axes.

TABLE II
EXTRACTED PARAMETERS FOR THE GLUCOSE LAYER

Time (hours)	Refractive index, $n_3(f = 0.7\ \text{THz})$	Extinction coefficient, $\kappa_3(f = 0.7\ \text{THz})$	Thickness, d_3 (μm)	Variational parameter, δ
60	2.06	0.13	244	0.076∠198°
70	2.05	0.12	242	0.096∠204°
80	2.03	0.11	240	0.102∠209°
90	2.02	0.10	239	0.103∠209°
100	1.98	0.10	239	0.096∠208°
110	1.93	0.09	237	0.089∠207°
120	1.92	0.09	236	0.082∠202°